PAPER

Methods to form atomically thin carbon coatings on SnS and SnO$_2$ nanostructures†

Shuankui Li,[ab] Jiaxin Zheng,[a] Shiyong Zuo,[b] Zhiguo Wu,[b] Pengxun Yan,[b] Andrey L. Rogach*[c] and Feng Pan*[a]

We report a citric acid-assisted solvothermal method to construct C@SnS@C sandwich nanosheets, which assemble into 3D porous microspheres. Citric acid plays a key role in both controlling the growth of the thin (5 nm) SnS nanosheets by absorption on the (100) SnS surface, and in the formation of an amorphous atomically thin carbon (ATC) layer (0.8 nm) on the surface of SnS nanocrystals through carbonization. The C@SnS@C sandwich nanosheets are used as precursors to form porous microsphere SnO$_2$@ATC composites, with the SnO$_2$ nanoparticles (10–20 nm) grown on the extended carbon framework. We demonstrate how the synergetic effect of the high theoretical lithium storage capacity of SnO$_2$ and electrical conductivity of the atomically thin carbon framework renders this composite a promising anode material for lithium ion batteries with enhanced capacity and superior cycling performance.

Introduction

Inorganic nanostructures have been extensively studied over the last decade, owing to their fascinating physical properties governed by both dimensionality and quantum size effects, and applicability prospects in many fields such as catalysis, energy storage and conversion, and optoelectronic devices.[1–3] Tin based compound semiconductors nanostructures such as SnS, SnSe, SnS$_2$, and SnO$_2$, have attracted great attention owing to their anticipated applications in many fields such as solar cells, field effect transistors, photodetectors, electrochemical capacitors, Li ion battery anodes and photocatalysis.[4–12] Extensive research studies have focused on their design to explore their structure-dependent properties and potential applications.[13–15] Various tin based compound nanostructures, such as 1D nanowire, 2D nanosheet, and 3D nanoflower have been extensively studied.[16–18] Their combination with amorphous carbon or graphene have been regarded as an efficient approach to improve its electrochemical performance as an anode material for lithium ion batteries, where the synergy between the functions of the two materials, high capacity of *i.e.* SnO$_2$ and good electronic conductivity of carbon/graphene to generate the high lithium ions diffusion efficiency has been exploited.[19] However,

most synthetic methods towards such hybrid structures require templates or surfactants, resulting in multi-step and costly fabrication. This calls for simple, reliable and economical synthetic routes for their construction.

Herein, we report a citric acid-assisted solvothermal strategy towards C@SnS@C composite nanostructures; formed from the thin (5 nm) SnS nanosheets sandwiched between atomically thin (0.8 nm) carbon (ATC) layers by carbonization of the citric acid. Using this composite material as a precursor, porous SnO$_2$@ATC microspheres composed of SnO$_2$ nanoparticles grown on ATC framework have been prepared. In this 3D architecture, the intimate contact between SnO$_2$ nanoparticles and ATC effectively prevents aggregation of SnO$_2$ nanoparticles and restrains the cracking of the electrode, while the continuous conductive matrix of 3D ATC framework facilitates electron transport through the electrode. Combined with the high theoretical lithium storage capacity of SnO$_2$, it makes SnO$_2$@-ATC composites promising lithium-ion battery anodes.

Experimental

3D porous microspheres constructed from C@SnS@C nanosheets

All the reagents were analytical grate and used without further purification. 226 mg of SnCl$_2$·2H$_2$O (1 mmol), 228 mg of CH$_4$N$_2$S (3 mmol) and 226 mg of citric acid were dissolved in 30 mL of propanetriol solution under magnetic stirring. The resulting solution was transferred into a Teflon-lined stainless autoclave (40 mL capacity), followed by solvothermal treatment at 190 °C for 18 h. The product was collected by filtration, successively washed several times with deionized water and absolute ethanol, and dried at 60 °C for 24 h.

a School of Advanced Materials, Peking University Shenzhen Graduate School, Shenzhen, 518055, China. E-mail: panfeng@pkusz.edu.cn; Tel: +86-755-26033200

b School of Physical Science and Technology, Lanzhou University, Lanzhou, Gansu, 730000, China. E-mail: zgwu@lzu.edu.cn; Fax: +86-931-8913554; Tel: +86-931-8912719

c Department of Physics and Materials Science and Centre for Functional Photonics, City University of Hong Kong, Hong Kong S.A.R., China

SnO₂@ATC composites

30 mg of glucose were dissolved in 30 mL of deionized water, and 30 mg of 3D porous microspheres constructed from C@SnS@C sandwich nanosheets was added into the solution under vigorous magnetic stirring. The resulting suspension was sealed into a 40 mL Teflon-lined autoclave, followed by hydrothermal treatment at 180 °C for 12 h. After the treatment, the products were collected by filtration, successively washed several times with deionized water and absolute ethanol, and dried at 60 °C for 24 h.

Characterisation

X-ray diffraction (XRD) was performed on a Philips X'Pert Pro Diffractometer; field-emission scanning electron microscopy (SEM) on a Hitachi S-4800 instrument; transmission electron microscopy (TEM) on a JEOL-2010 instrument. Nitrogen adsorption–desorption isotherms were measured on a ASAP 2010 sorption analyzer at 77 K. Specific surface area was calculated by the BET (Brunauer–Emmett–Teller) method, and the pore size distribution was calculated from the adsorption branch using the BJH (Barrett–Joyner–Halenda) method. CR2016 type half cells were assembled in a high-purity argon-filled glove box from SnO₂@ATC composites as the anode material. The anodes were prepared by mixing SnO₂@ATC, carbon black, and polyvinylidene difluoride at a weight ratio of 85 : 10 : 5 in N-methyl-2-pyrrolidone (NMP) solvent. The loading density on a Cu foil was ~1.5 mg cm⁻². A Li foil was used as the cathode. LiPF₆ (1 M) in ethylene carbonate/diethyl carbonate (1 : 1 w/w) was used as the electrolyte. The charge/discharge tests were performed using a multi-channel battery workstation (Lande Co., China).

Results and discussion

For the orthorhombic SnS, the most stable facets are (100), due to the strongest ionic interactions.[20–22] As illustrated in Fig. 1 and S1a,† this results in an anisotropic growth of SnS with the (100) facets becoming mostly exposed. On the other hand,
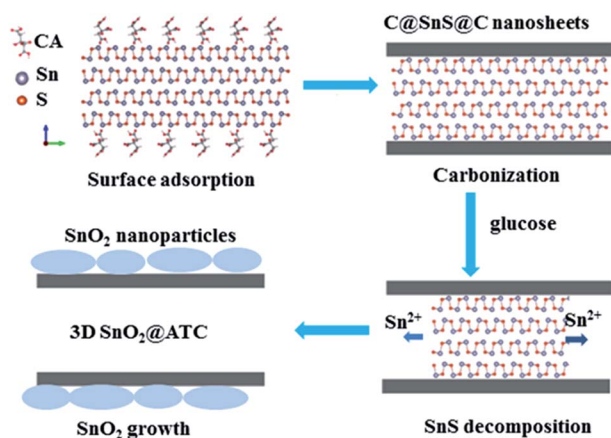
selective surface adsorption of solvent or additives molecules is crucial to the equilibrium shape transformation.[23–25] The adsorption of citric acid on the (100) SnS surface has been found to be stronger than for the solvent propanetriol, leading to a more stable citric acid/SnS (100) surface, and resulting in thinner SnS nanosheets, as confirmed by calculating the adsorption of propanetriol *versus* citric acid on SnS (100) surface (Fig. S1b†). COOH groups of citric acid form bi-dentate bridges between Sn and S atoms (–C=O⋯Sn and –COH⋯S bonds) on the (100) SnS surface, as shown in Fig. S1b.† The directional alignment of citric acid molecules then takes place on the (100) SnS surface which, combined with a net structure supported by the hydrogen bonds, leads to a stable citric acid-terminated (100) SnS surface. From these considerations, we identified citric acid as an appropriate additive to tune the thickness of the SnS sheets during the solvothermal growth process. Moreover, under the high temperature solvothermal conditions, a carbonization process can take place, which transforms adsorbed citric acid molecules into atomically thin carbon (ATC) layers on SnS nanosheet surface, as schematically illustrated in Fig. 1. The interface with SnS additionally assists the carbonization of citric acid, which has been confirmed by a series of control experiments.

Fig. 3a and b show SEM images of the resulting 3D porous microspheres constructed from C@SnS@C sandwich nanosheets. The TEM image (Fig. 3c) shows that the thicknesses of nanosheets is in the range of 4–10 nm. HRTEM images of both top view and side view of a SnS nanosheet (Fig. 3d and e) confirm that sheets are single-crystalline with the normal of the primary surfaces along [100] direction. The XRD pattern (Fig. 2) of 3D porous microspheres constructed from C@SnS@C sandwich nanosheets indexed them as α-SnS (JCPDS card no. 39-0354), which is in a good agreement with literature.[26,27] No other impurity peaks are observed indicating the high purity of the as-synthesized material. The very high peak intensity

Fig. 1 Schematic illustration of the citric acid (CA) assisted formation of C@SnS@C sandwich nanosheets and of SnO₂@ATC composites.
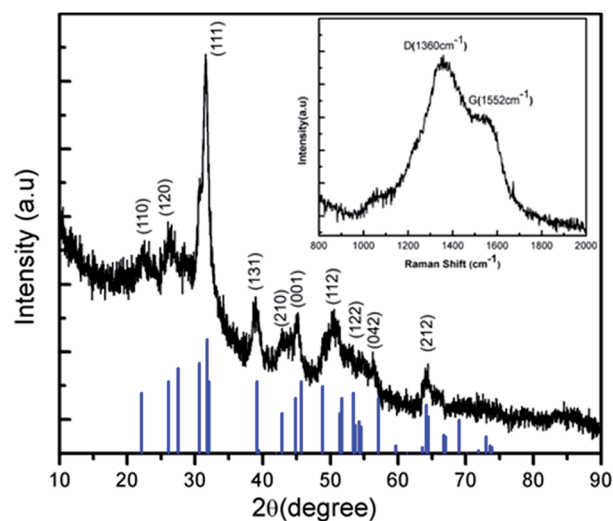
Fig. 2 XRD pattern of 3D porous microspheres assembled from C@SnS@C sandwich nanosheets. The blue line spectrum gives XRD pattern of α-SnS (JCPDS card no. 39-0354). The inset is the Raman spectra of the sample.
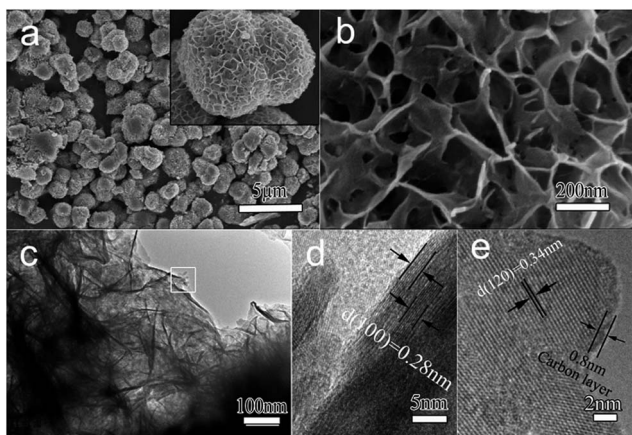
Fig. 3 SEM (a, b) and TEM (c) images of 3D porous microspheres constructed from C@SnS@C sandwich nanosheets. HRTEM images (d) and (e) show top and side view of planar nanosheets, respectively.

Fig. 4 SEM (a, b) and TEM (c, d) images of the 3D porous SnO$_2$@ATC composite. HRTEM image of a fragment of the structure is presented in (e).

suggests that the material is well crystallized. HRTEM also clearly revealed the presence of the amorphous coating on the surface of SnS nanosheets, with the thickness of 0.8 nm (Fig. 3e). To verify the chemical nature of this coating to be amorphous carbon, EDX elemental mapping has been performed, and showed a uniform presence of carbon over the SnS microspheres, alongside with other two elements Sn and S (Fig. S2†). The presence of carbon in the composite material was further confirmed by Raman spectra (inset in Fig. 2), with signatures of both G band ($\sim$1552 cm^{-1}) and D band ($\sim$1350 cm^{-1}) of poorly crystallized carbon similar to the one formed by carbonization of organic surfactants under solvothermal conditions.[28] Thus, we conclude that we indeed obtained 3D porous microspheres constructed from C@SnS@C sandwich nanosheets, as illustrated by the scheme of Fig. 1.

In the next processing step, these microspheres were used as precursors to fabricate porous SnO$_2$@ATC composites with SnO$_2$ nanoparticles grown on 3D ATC framework, as a result of the hydrothermal treatment in the glucose aqueous solution (scheme in Fig. 1). As demonstrated by SEM images in Fig. 4a and b, compared to Fig. 3a and b, the resulting microspheres became even more porous than the precursor ones, and they appear as composed of numerous interconnected small (10–20 nm) nanoparticles distributed over the surface (TEM image in Fig. 4c). These nanoparticles are supported by amorphous (carbon) framework, as can be observed at the edge of the nanosheet as shown in Fig. 4d. The HRTEM image in Fig. 4e revealed lattice planes with the interplanar distance of 0.34 nm for these nanoparticles, corresponding to the (110) plane of SnO$_2$ cubic crystalline structure. The amorphous nature of the carbon framework is pointed out by an arrow in Fig. 4e. In the XRD pattern of the composite (Fig. 5a), all the diffraction peaks can be indexed to crystalline SnO$_2$ (JCPDS no. 41-1445).

Fig. 1 schematically illustrates the possible formation mechanism of SnO$_2$@ATC composite as a result of SnS decomposition process in an acidic glucose solution. Under acidic conditions, SnS releases Sn^{2+} ions which react with glucose and OH$^-$ to form SnO$_2$ nuclei on the surface of the
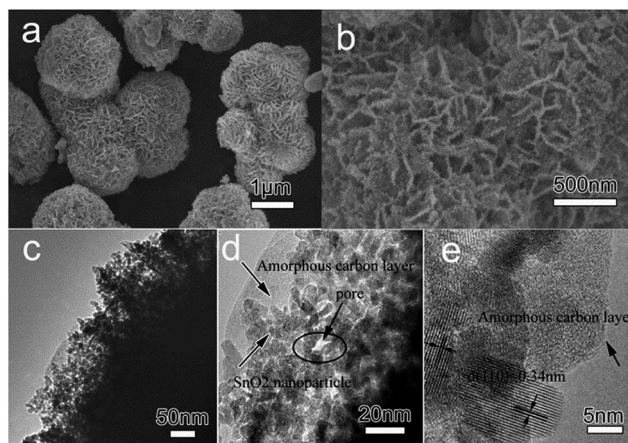
carbon framework. Thermo-gravimetric analysis (TGA) was employed to determine the carbon content in the SnO$_2$@ATC composite. The TGA curve Fig. 5b reveals that the decomposition of amorphous carbon takes place between 400 °C and 600 °C, and the carbon content in the SnO$_2$@ATC composite is $\sim$4.5 wt%, which is slightly higher than for the C@SnS@C precursor ($\sim$3.1 wt%). This means that the glucose partially transforms into carbon during the hydrothermal treatment. From the BET analysis (Fig. 5c and d), it was found that the 3D porous SnO$_2$@ATC composite has surface area of 67 m^2 g^{-1}, which is larger than for C@SnS@C microsphere precursor (51 m^2 g^{-1}). The pore-size distribution curve of the microsphere precursor
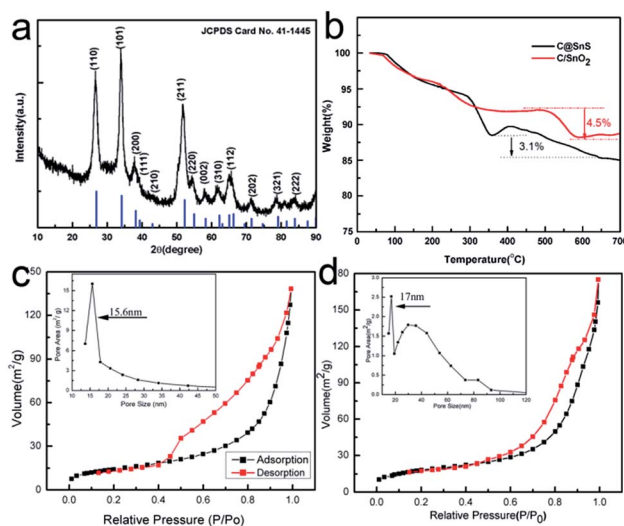
Fig. 5 (a) XRD pattern of the SnO$_2$@ATC composite. The blue line spectrum gives XRD pattern of the crystalline SnO$_2$ (JCPDS no. 41-1445). (b) Thermogravimetric analysis of the porous microspheres constructed from C@SnS@C sandwich nanosheets (black) and SnO$_2$@ATC composite (red). Nitrogen adsorption−desorption isotherms and the corresponding pore size distributions (insets) for (c) 3D porous microspheres assembled from C@SnS@C sandwich nanosheets and (d) SnO$_2$@ATC composite.

exhibited one narrow peak located at 16 nm, which is most probably related to the interstices between adjacent nanosheets as observed in the SEM and TEM images in Fig. 3. In contrast, the pore-size distribution curve of the SnO₂@ATC composite had bimodal shape with a narrow peak located at 17 nm and a broad one centered at 40 nm. The 17 nm peak can be ascribed to the interstices within the 3D carbon framework, and the another one to pores between SnO₂ nanoparticles.

3D porous SnO₂@ATC composite with high-density SnO₂ nanoparticles grown on the surface of carbon framework may exhibit enhanced lithium storage, providing not only a large area for lithium insertion/extraction but also ensuring a short solid-state diffusion length. Recently, a similar nanostructure comprising MoS₂ nanosheets attached to the carbon nanosheets demonstrated an outstanding long-life cycling performance at high rates.[29] The uniform and continuous ATC framework can remarkably enhance the electrical conductivity leading to the formation of thin solid electrolyte interface films on the electrode surface, and at the same time provides a continuous conductive path between SnO₂ nanoparticles, thus reducing the particle-to-particle interface resistance.[30,31] The presence of SnO₂ nanoparticles with a small size of 10–20 nm can significantly shorten the diffusion distance of Li⁺ ions, and therefore significantly enhance the lithium insertion–extraction kinetics. The 3D porous structure with plenty of slit-like void space can easily be filled with the electrolyte, ensuring a high surface area being in contact with the electrolyte, and hence a large flux of Li⁺ across the interface. Additionally, both the ATC framework and the interstices between adjacent SnO₂ nanoparticles provide elastic buffer space to accommodate the volume changes upon Li ion insertion/extraction, which would restrain the cracking of the electrode and lead to superior cycling performance.[32]

According to previous reports, the lithium intercalation and conversion reactions based on the formation of metallic Sn and subsequent generation of a Li–Sn alloy, which could be demonstrated by the cyclic voltammetry curves (Fig. 6a). The discharge–charge profiles of the 3D porous SnO₂@ATC anode (Fig. 6b) revealed an initial discharge capacity of 1486 mA h g⁻¹ and the initial recharge capacity of 647 mA h g⁻¹. The second discharge capacity was found to be 769 mA h g⁻¹, which constitutes 98% of the maximum theoretical reversible capacity of SnO₂ (Fig. 6c). The decomposition of SnO₂ into metallic Sn and Li₂O as well as the formation of solid electrolyte interface (SEI) may lead to the large irreversibility of Sn-based anodes at the first charge/discharge cycle, which has been often reported in literature.[30,32] The anode maintained a reversible discharge capacity of 652 mA h g⁻¹ after 50 cycles, which is much higher than that of the collapsed C/SnO₂ nanosheets obtained under high glucose concentration (at a current density of 100 mA g⁻¹, the specific capacity of the porous C/SnO₂ nanosheets is 678 mA h g⁻¹ during the 2th cycle, which decays to 300 mA h g⁻¹ during the 50th cycle, Fig. S3†). This means that the 3D ATC framework is essential to maintain the large capacity of 3D porous SnO₂@ATC composites. In order to demonstrate the stability of the SnO₂@ATC electrode, the morphological changes in representative electrodes after 50 cycles were examined using SEM.
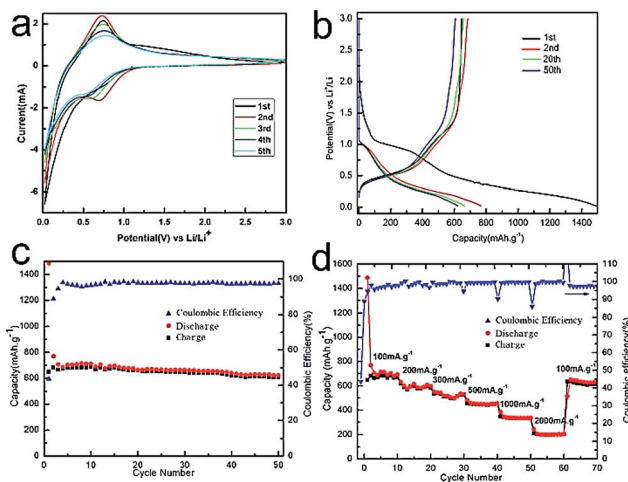
Fig. 6 Electrochemical performance of the 3D porous SnO₂@ATC composite electrode: (a) cycle voltammograms at a scan rate of 2 mV s⁻¹; (b) the 1st, 2nd, 20th and 50th discharge/charge profiles at a current density of 100 mA g⁻¹; (c) cyclic performance and coulombic efficiency at a current density of 100 mA g⁻¹ for 50 cycles; (d) rate performance at different current densities.

Fig. S4a and b† show that the 3D porous architecture is retained after 50 cycles at 100 mA g⁻¹, which confirmed the excellent structural stability of the as-prepared materials. The 3D porous ATC framework provide elastic buffer space to accommodate the volume changes upon Li ion insertion/extraction, which would restrain the cracking of the electrode and lead to superior cycling performance. The 3D porous SnO₂@ATC composite also exhibited excellent rate capability, as demonstrated in Fig. 6d. Its discharge capacity reached 682 mA h g⁻¹ after the first 10 cycles at a low current density of 100 mA g⁻¹, and then reduced to 631, 551, 481, 385 and 209 mA h g⁻¹ at current density of 200, 300, 500, 1000, and 2000 mA g⁻¹, respectively. Even at the current density as high as 2000 mA g⁻¹, the electrode delivered a capacity higher than 209 mA h g⁻¹. More importantly, when the current density returned to the initial value of 100 mA g⁻¹ after 51 cycles, the electrode recovered its original capacity (670 mA h g⁻¹ in the 70th cycle). These results indicate that the 3D porous SnO₂@ATC composite, with its high capacity and stable cycling performance, is very promising anode material for the rechargeable lithium ion batteries.

Conclusions

In conclusion, based on the theoretical considerations of the stabilities of (100) SnS facets with an adsorbed monolayer of citric acid molecules, we developed a citric acid-assisted solvothermal strategy to prepare porous microspheres constructed from C@SnS@C sandwich nanosheets. The role of citric acid is not only to allow for formation of thin (5 nm) SnS nanosheets, but also to form an amorphous ATC layer (0.8 nm thin) by carbonization. Microspheres composed of C@SnS@C nanosheets were used as precursors to fabricate the 3D porous SnO₂@ATC composites with SnO₂ nanoparticles grown on the carbon framework under hydrothermal treatment in the

presence of glucose. The anodes based on these composites exhibited highly reversible capacity (650 mA h g^{-1} after 50 cycles), good cycle ability and rate capability for lithium-ion batteries. We also note that the fabrication strategy of ACT layers introduced in this work can be extended to the construction of other nanostructures of metal sulfides/oxides anchored on carbon frameworks for different applications.

Acknowledgements

Notes and references

1 X. Zhang and Y. Xie, *Chem. Soc. Rev.*, 2013, **42**, 8187–8199.

2 Y. Sun, S. Gao and Y. Xie, *Chem. Soc. Rev.*, 2014, **43**, 530–546.

3 M. Xu, T. Liang, M. Shi and H. Chen, *Chem. Rev.*, 2013, **113**(5), 3766–3798.

4 L. W. Ji, H. L. Xin, T. R. Kuykendall, S. L. Wu, H. M. Zheng, M. M. Rao, E. J. Cairns, V. Battagliac and Y. G. Zhang, *Phys. Chem. Chem. Phys.*, 2012, **14**, 6981–6986.

5 X. H. Yang, T. Song, S. Lee, H. Han, F. Xia, A. Devadoss, W. Sigmund and U. Paik, *Electrochim. Acta*, 2013, **91**, 275–281.

6 L. D. Zhao, S.-H. Lo, Y. S. Zhang, H. Sun, G. J. Tan, C. Uher, C. Wolverton, V. P. Dravid and M. G. Kanatzidis, *Nature*, 2014, **508**, 373–377.

7 I. T. Sines, D. D. Vaughn, A. J. Biacchi, C. E. Kingsley, E. J. Popczun and R. E. Schaak, *Chem. Mater.*, 2012, **24**(15), 3088–3093.

8 P. Sinsermsuksakul, L. Sun, S. W. Lee, H. H. Park, S. B. Kim, C. Yang and R. G. Gordon, *Adv. Energy Mater.*, 2014, **4**(15), 1400496.

9 J. Liang, X.-Y. Yu, H. Zhou, H. B. Wu, S. J. Ding and X. W. Lou, *Angew. Chem., Int. Ed.*, 2014, **53**, 12803–12807.

10 H. Wang, K. Dou, W. Y. Teoh, Y. Zhan, T. Hung, F. F. Zhang, J. Xu, R. Zhang and A. L. Rogach, *Adv. Funct. Mater.*, 2013, **23**, 4847–4853.

11 H. Wang, F. Fu, F. Zhang, H.-E. Wang, S. V. Kershaw, J. Xu, S.-G. Sun and A. L. Rogach, *J. Mater. Chem.*, 2012, **22**, 2140–2148.

12 H. Wang and A. L. Rogach, *Chem. Mater.*, 2014, **26**, 123–133.

13 C. Kim, M. Noh, M. Choi, J. Cho and B. Park, *Chem. Mater.*, 2005, **17**, 3297–3301.

14 H. J. Ahn, H. C. Choi, K. W. Park, S. B. Kim and Y. E. Sung, *J. Phys. Chem. B*, 2004, **108**, 9815–9820.

15 Y. Wang, J. Y. Lee and H. C. Zeng, *Chem. Mater.*, 2005, **17**, 3899–3903.

16 X. W. Lou, L. A. Archer and Z. Yang, *Adv. Mater.*, 2008, **20**, 3987–4019.

17 Z. Wang, D. Luan, F. Boey and X. W. Lou, *J. Am. Chem. Soc.*, 2011, **133**, 4738–4741.

18 Y. F. Sun, Z. H. Sun, S. Gao, H. Cheng, Q. H. Liu, F. C. Lei, S. Q. Wei and Y. Xie, *Adv. Energy Mater.*, 2014, **4**, 1300611–1300622.

19 D. Wang, J. Yang, X. Li, D. Geng, R. Li, M. Cai, T. Sham and X. A. Sun, *Energy Environ. Sci.*, 2013, **6**, 2900–2906.

20 A. J. Biacchi, D. D. Vaughn and R. E. Schaak, *J. Am. Chem. Soc.*, 2013, **135**, 11634–11644.

21 Y. J. Zhang, J. Lu, S. L. Shen, H. R. Xu and Q. B. Wang, *Chem. Commun.*, 2011, **47**, 5226–5228.

22 J.-G. Kang, J.-G. Park and D.-W. Kim, *Electrochem. Commun.*, 2010, **12**, 307–310.

23 J. S. Zhu, D. L. Wang and T. F. Liu, *Ionics*, 2014, **20**, 141–144.

24 D. D. Vaughn II, O. D. Hentz, S. Chen, D. Wang and R. E. Schaak, *Chem. Commun.*, 2012, **48**, 5608.

25 J. Lu, C. Y. Nan, L. H. Li, Q. Peng and Y. D. Li, *Nano Res.*, 2013, **6**(1), 55–64.

26 P. Sinsermsuksakul, K. Hartman, S. B. Kim, J. Heo, L. Sun, H. H. Park and R. G. Gordon, *Appl. Phys. Lett.*, 2013, **102**(5), 053901.

27 J. Vidal, S. Lany, M. d'Avezac, A. Zunger, A. Zakutayev and J. Francis, *Appl. Phys. Lett.*, 2012, **100**(3), 032104.

28 Y. T. Zhong, X. Wang, K. C. Jiang, J. Y. Zheng, Y. G. Guo, Y. Ma and J. N. Yao, *J. Mater. Chem.*, 2011, **21**, 17998–18002.

29 J. W. Zhou, J. Qin, X. Zhang, C. S. Shi, E. Z. Liu, J. J. Li, N. Q. Zhao and C. N. He, *ACS Nano*, 2015, **9**(4), 3827–3848.

30 G. Gao, H. B. Wu, S. Ding and X. W. Lou, *Small*, 2015, **11**, 432–436.

31 C. Guan, X. Wang, Q. Zhang, Z. Fan, H. Zhang and H. J. Fan, *Nano Lett.*, 2014, **14**(8), 4852–4858.

32 Y. Huang, D. Wu, J. Wang, S. Han, L. Lv, F. Zhang and X. Feng, *Small*, 2014, **10**(11), 2226–2232.